Available online at www.sciencedirect.com
ScienceDirect
Ocean Modelling 18 (2007) 194–209
Ocean Modelling
www.elsevier.com/locate/ocemod

Open boundary conditions for regional tidal simulations

Glenn S. Carter *, Mark A. Merrifield

Department of Oceanography, University of Hawai'i at Manoa, 1000 Pope Road, Honolulu, HI 96822, USA

Received 17 November 2006; received in revised form 23 April 2007; accepted 23 April 2007
Available online 10 May 2007

Abstract

The performance of regional tide model simulations is examined in relation to the choice of open boundary conditions. Three barotropic open boundary conditions, clamped elevation, clamped normal velocity, and Flather, give similar results when the prescribed values are exact; however, Flather is much less sensitive to errors in the prescribed values. Of particular concern, it was found that with a phase error between the two boundaries, both the clamped conditions resulted in magnitude errors in the unclamped variable (although the simulation remained stable).

A modified flow relaxation scheme for the depth-varying prognostic variables is presented. This implementation allows the transmission of a range of vertical modes while retaining realistic topography at the boundary. It was found to be an excellent internal tide boundary condition in tests comparing simulations of different domain length encompassing a ridge and sloping bottom, and in a comparison to an analytical solution. Mass is conserved without any artificial volume constraint.

Published by Elsevier Ltd.

Keywords: Open boundary conditions; Modeling; Tidal modeling

1. Introduction

Recently, there has been a resurgence of interest in open-ocean tidal processes. Much of this has been driven by satellite observations showing nearly 1 TW of energy is removed from the barotropic tide in regions away from shallow seas (Egbert and Ray, 2000, 2001) and that baroclinic (internal) tides can propagate hundreds of kilometers from their generation regions (Dushaw et al., 1995; Ray and Mitchum, 1996; Cummins et al., 2001). As well as being a main contributor to global ocean energetics, tides play an obvious and important role in many coastal processes.

Process studies utilizing regional numerical simulations have been employed alongside observations and theory in an effort to understand tidal problems. These simulations are increasingly being used to extrapolate *in situ* observations of quantities such as energy flux (Rudnick et al., 2003; Lee et al., 2006) and dissipation (Klymak et al., 2006; Carter et al., 2006) as well as state variables. Large programs such as the Hawaii Ocean

* Corresponding author. Tel.: +1 808 956 9267; fax: +1 808 956 2352.
E-mail addresses: gscarter@hawaii.edu (G.S. Carter), markm@soest.hawaii.edu (M.A. Merrifield).

1463-5003/$ - see front matter Published by Elsevier Ltd.
doi:10.1016/j.ocemod.2007.04.003

Mixing Experiment (HOME, Pinkel et al., 2000) allow the comparison of numerical simulations to observations at a range of scales. Accordingly, the definition of good agreement between simulation and observations is evolving to accommodate these new uses.

Open boundary conditions (OBCs), which must be prescribed to complete the model description at non-land boundaries, have a large effect on the simulation. The definition of these boundary conditions is not trivial, in fact for incompressible, hydrostatic primitive equation models they are known to make the system ill-posed (Oliger and Sundström, 1978). OBCs can be broadly divided into two classes, passive and active (Palma and Matano, 1998). Passive boundary conditions, which aim to let information exit the model domain without reflection, have been the subject of a number of studies (e.g., Chapman, 1985; Jensen, 1998; Palma and Matano, 1998, 2000). Passive boundary simulations include adjustment of an initial discontinuity, along- or across-shelf wind stress and the response to a passing storm. Active boundary conditions, on the other hand, are used to drive the simulation, and have been less well studied. Marchesiello et al. (2001) proposed a combination, an adaptive boundary condition, where different definitions are used depending on whether information is entering or leaving the domain.

One of the difficulties with OBCs is that their performance has been found to be highly dependent on the simulation configuration. This current study of OBC was motivated by our interest in internal tide dynamics near (within $\approx$100 km of) a generation region. Process studies using realistic topography, realistic but horizontally constant stratification, and reduced forcing (typically one or two constituents) are an informative and common approach (Merrifield et al., 2001; Niwa and Hibiya, 2001; Merrifield and Holloway, 2002; Holloway and Merrifield, 2003; Johnston et al., 2003). The OBC comparison studies to date have not addressed tidal forcing. Depending on the topography and stratification, internal tide generation can transfer energy to a wide range of vertical modes (Garrett and Kunze, 2007) each with a different phase speed, and even form tidal beams through the phase-locking of multiple modes (e.g., Prinsenberg et al., 1974). St Laurent et al. (2002) suggest $30 \pm 10\%$ of the energy converted into internal tides can go into high modes.

1.1. Numerical model

In this analysis we use the Princeton Ocean Model (POM), a three-dimensional, non-linear, free surface, time stepping, primitive equation model originally developed for coastal applications (Blumberg and Mellor, 1987). It has subsequently been used in a number of barotropic and baroclinic tidal studies, including idealized open-ocean topographic features (e.g., Holloway and Merrifield, 1999; Johnston and Merrifield, 2003), two-dimensional representation of shelf topography (e.g., Holloway, 1996), and realistic three-dimensional topography (e.g., Merrifield et al., 2001; Niwa and Hibiya, 2001; Merrifield and Holloway, 2002; Holloway and Merrifield, 2003; Johnston et al., 2003). Palma and Matano (1998, 2000) used POM in an investigation of passive open boundary conditions.

The model equations and how they are solved is discussed in detail by Blumberg and Mellor (1987). Key details pertinent to this study are described here. POM uses a finite difference approach on a staggered (Arakawa C) grid, with curvilinear coordinates in the horizontal and sigma coordinates in the vertical. The differences are calculated explicitly in the horizontal and implicitly in the vertical. POM employs a mode splitting technique, whereby the vertically averaged velocities and free surface elevation (external mode) are calculated with a shorter time step than the depth-varying variables (internal mode). Mode splitting requires that boundary conditions are applied to both the external and internal modes.

2. External mode

There are three prognostic variables (η, $\bar{u}$, and $\bar{v}$; where the overbar denotes the vertical average) solved for in the external mode. At the boundaries some description must be given for each of these variables, however, if each of the three variables were set to an externally (user) prescribed value the model would, in all likelihood, be over-specified (i.e., the prescribed values would be incompatible with the interior equations; Marchesiello et al., 2001) and probably become unstable. In general, only one of the variables is prescribed and the other two are related to the interior model solution, here a zero gradient ($\phi_b = \phi_{\text{interior neighbor}}$) is used.

2.1. Boundary conditions

Although a large number of boundary conditions have been proposed for different situations (see Palma and Matano, 1998; Blayo and Debreu, 2005, for reviews), three types of barotropic boundary conditions tend to be used for tidal simulations:

- *Clamped elevation*: Here the free surface displacement is set to an externally prescribed value:

$$\eta_{b\pm1} = \eta^{\text{ext}}, \tag{1}$$

  where $\eta_{b\pm1}$ indicates that the elevation must be clamped one cell in from the boundary (Mellor, 2004). This continues to be a popular boundary condition for tidal simulations, due in part to the smooth spatial variation of elevation data, and readily available satellite-altimetry-derived data.
- *Clamped normal velocity*: This condition sets the normal velocity component in the boundary cell ($\bar{v}_{n,b}$) to an externally prescribed value:

$$\bar{v}_{n,b} = \bar{v}_n^{\text{ext}}. \tag{2}$$

- *Flather condition*: This extension of a radiation boundary condition was originally proposed by Flather (1976). Radiation conditions are a popular class of passive OBCs, which are based on the propagation of a quantity ψ through a boundary:

$$\frac{\partial \psi}{\partial t} + c\frac{\partial \psi}{\partial n} = 0, \tag{3}$$

  where n is the outward normal, and c is a velocity. The Flather condition is a combination of (3) applied to the free surface elevation, the long wave phase speed ($c = \sqrt{gH}$, where g is gravitational acceleration and H is bottom depth), and a one-dimensional approximation of the continuity equation:

$$\frac{\partial \eta}{\partial t} + H\frac{\partial \bar{v}_n}{\partial n} = 0, \tag{4}$$

  which gives

$$\frac{\partial}{\partial n}\left[\bar{v}_n - \frac{c}{H}\eta\right] = 0. \tag{5}$$

  Finally, integrating across the boundary gives

$$\bar{v}_{n,b} = \bar{v}_n^{\text{ext}} \pm \sqrt{\frac{g}{H}}(\eta_{b\pm1} - \eta^{\text{ext}}). \tag{6}$$

  The Flather condition can be thought of as applying an adjustment to the externally prescribed normal velocity based on the difference between modeled and externally prescribed surface elevations, i.e., a volume error. In POM the elevations are calculated prior to updating the external mode velocities, therefore $\eta_{b\pm1}$ is at the same timestep as $\bar{v}_{n,b}$. The sign of the adjustment velocity depends on the boundary (positive for north and east boundaries; negative for south and west boundaries).

For passive boundary conditions, it is well known that clamping results in very poor performance (Chapman, 1985). A clamped boundary condition is 100% reflective to any flow not described by the boundary condition. Despite this clamped conditions, particularly clamped elevation, remain popular as an active boundary condition for tidal simulations (e.g., Cheng et al., 1993; Holloway, 1996; Black et al., 2000; Merrifield et al., 2001; Merrifield and Holloway, 2002; Holloway and Merrifield, 2003; Katsumata, 2005; Banas and Hickey, 2005).

Blayo and Debreu (2005) showed that the Flather condition is a characteristic solution to the 2D linearized inviscid shallow-water equations, i.e., forms a well-posed problem. The primitive equations are not hyperbolic and consequently the Flather condition is not a characteristic solution, although in comparison tests of passive OBCs the Flather condition is amongst the best performers (Palma and Matano, 1998). Marchesiello et al. (2001) found that in a simulation of the west coast of the United States, a barotropic rim current was set

up by the Flather condition. In primitive equation models the Flather condition seems most suited to situations where surface gravity waves dominate (Marchesiello et al., 2001).

2.2. Approach

The simplest possible tidal configuration, a freely propagating sinusoidal long wave in a constant depth channel, is considered. The continuity and momentum equations in this case reduce to (Pugh, 1987)

$$\frac{\partial \eta}{\partial t} + H\frac{\partial \bar{u}}{\partial x} = 0, \tag{7}$$

$$\frac{\partial \bar{u}}{\partial t} + g\frac{\partial \eta}{\partial x} = 0, \tag{8}$$

which has solutions

$$\eta = \eta_0 \cos(kx - \omega t) = \eta_0 \cos(\omega t + \phi), \tag{9}$$

$$\bar{u} = \eta_0 \sqrt{\frac{g}{H}} \cos(kx - \omega t) = \eta_0 \sqrt{\frac{g}{H}} \cos(\omega t + \phi), \tag{10}$$

where η_0 is the amplitude of the surface oscillation, ω is the frequency, k is the wavenumber, and ϕ is the phase. The phase difference between the ends of the channel (L apart) is governed by the travel time of the wave, and is given by

$$|\Delta\phi| = L\omega/c \text{ [radians]}. \tag{11}$$

The majority of simulations presented in this section are 2D runs of a 250 cell long east–west channel with horizontal grid spacing of 2 km, a constant depth of $H = 4500$ m, and the Coriolis force set to zero (no rotation). The external forcing is an eastward propagating M_2 frequency wave with $\eta^{\text{ext}} = 2$ m and $\bar{u}^{\text{ext}} = 2\sqrt{g/H} \cong 0.09$ m s^{-1}. To enforce the unidirectional flow on a tidal channel the normal velocity on the north and south boundaries is set to zero (this is equivalent to a wall). All the tangential velocity components are set using a zero gradient. Each simulation is run for 60 tidal cycles (~31 days) starting from a quiescent state, with forcing gradually increasing over one day to minimize the adjustment through waves. Singular value decomposition (Press et al., 1989) is used to evaluate the mean (offset from the initial water-level) and harmonic constants (amplitude and phase) over the last 10 tidal cycles.

The theoretical momentum balance, (8), does not include a frictional term. The horizontal diffusivity in the model has been set to zero. However, POM calculates the bottom friction coefficient using a logarithmic layer formulation:

$$c_{\text{bottom}} = \left(\frac{\kappa}{\log(\delta z_b H / z0_b)}\right)^2, \tag{12}$$

where κ is von Karman's constant, δz_b is the distance between the deepest velocity level and the seabed, H is the water depth, and $z0_b$ is the bottom roughness. This should be small for deep channels. To confirm that bottom friction plays a negligible role in these simulations, and hence that it should be possible to directly compare with the inviscid theoretical solutions, a non-oscillating run was made with a 1 mm difference in elevation between the two ends of the domain. The forcing was gradually increased over one day from a quiescent state. After 120 days the along-channel velocity was still increasing, although approaching its asymptotic value where the friction in the model balances acceleration (Fig. 1). After 60 tidal cycles the model velocity is almost equal to the theoretical inviscid velocity ($g\frac{\partial \eta}{\partial x}t$), meaning close agreement between the simulations and (9) and (10) should be possible.

2.3. Results from the simple tidal channel

When both boundaries are set to the theoretical values, all three OBCs give very good agreement to Eqs. (9) and (10). Comparing the harmonic constants for the middle cell of the domain, however, shows that the

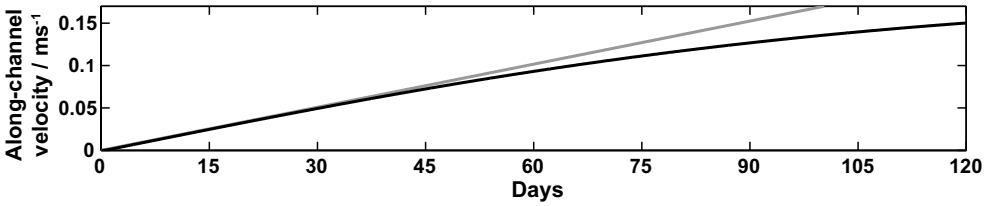

Fig. 1. Along-channel velocity in a non-oscillating simulation with a 1 mm elevation difference along the 500 km channel: Black line, POM simulation; and gray line theoretical value. After 120 days the small bottom friction in the model formulation had not completely balanced the acceleration.

Table 1
Comparison of the clamped elevation, clamped normal velocity, and Flather boundary conditions for a freely propagating tide in a constant depth channel, and the imposed boundary conditions exactly match theory

OBC	η / m			$\bar{u}$ / m s^{-1}		
	Mean	Amp		Mean	Amp	
		Value	%Error		Value	%Error
Clamped η	0.000	2.000	0.0	−0.001	0.094	0.8
Clamped $\bar{v}_n$	−0.027	2.008	0.4	0.000	0.093	0.0
Flather	0.000	2.000	0.0	0.000	0.093	0.0

Values are from the harmonic analysis on the center cell of the domain. Percentage errors are defined as $100[(\Phi^{\text{harmonic}} - \Phi^{\text{ext}})/\Phi^{\text{ext}}]$, where $\Phi = \eta$ or $\bar{u}$.

Flather condition is the most accurate (Table 1). The two clamped boundary conditions have small errors in the unclamped variable. In terms of amplitude these errors range from 0.4% to 0.8%, and an offset of <1% of the forcing amplitude is also introduced. $\bar{v}$ is identically zero with all three OBCs.

As it is unrealistic to assume that perfectly consistent boundary values would be available for all simulations, it is important to quantify the sensitivity of the various OBCs to errors in the externally prescribed values. Here we consider two possible classes of errors that may arise in measurement derived boundary conditions. Errors in travel time, or phase, across the domain, and errors in the amplitude of either η^{ext} or $\bar{u}^{\text{ext}}$.

To examine the sensitivity of the tidal simulations to phase errors at the boundaries, we conduct a series of runs where the phase at the western boundary is held at zero and the eastern boundary is $-|\Delta\phi| + \epsilon_\phi$, where ϵ_ϕ ranges from $-90°$ to $90°$. Similar to the exact OBC case, the Flather condition gives the best results and the clamped boundary conditions result in errors, particularly in the unclamped variable (Fig. 2). Regardless of the phase error, the Flather condition gives zero mean offset (Fig. 2a and b) and zero M_2 harmonic amplitude errors as a percentage of the theoretical value (Fig. 2c), i.e., agreement with theory. This is consistent with the interpretation of Blayo and Debreu (2005) that the Flather condition 'imposes the value of the incoming characteristic of the shallow-water equation', and hence the tidal wave can propagate cleanly through the outgoing boundary.[1]

The response of the two clamped OBCs is nearly symmetric (Fig. 2). Both OBCs give no mean offset in the clamped variable, and the percentage amplitude error in elevation for the clamped velocity condition is almost equal to the error in velocity for the clamped elevation case. There is, however, a 30-fold difference in mean offset for the unclamped variables, with clamped elevation resulting in a smaller offset than clamped velocity. Unlike the Flather OBC, there is also some along-channel variability ($\lesssim 5\%$).

Of real concern is the amplitude errors in the unclamped variable, which range from 0.05 to 5 times the theoretical value. For example, with an error of $+20°$ (5.5%) the magnitude of the unclamped variable is twice

[1] Our POM simulations indicate that for a pure channel the eastern boundary is always treated as the outgoing boundary. Attempts to simulate a westward propagating tide in the channel still result in an eastward propagating wave, with the phase at the western boundary determined from the external conditions. However, when the tidal wave is at an angle to the grid, there is sufficient phase information for the Flather condition to determine the wave direction and correctly identify the outgoing boundary.

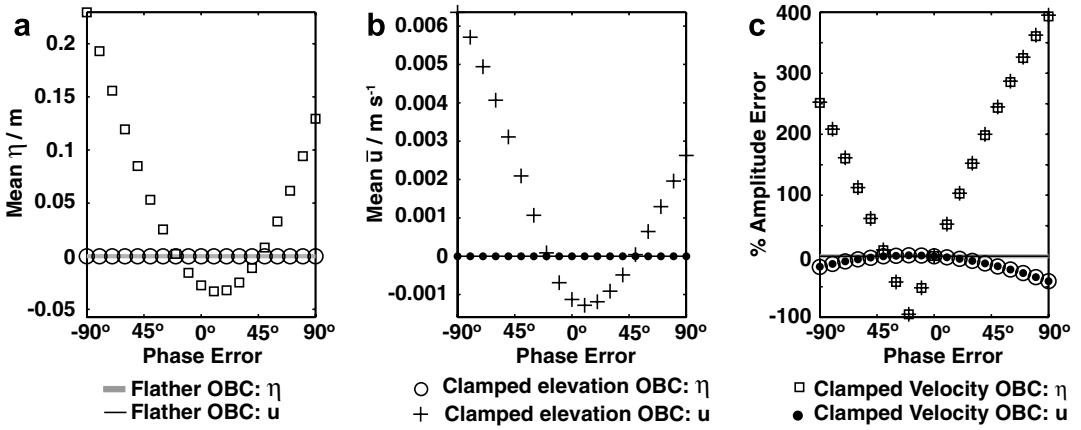

Fig. 2. Sensitivity of tidal channel simulations to errors in phase between the west and east boundaries. All values are from the harmonic fits to the middle grid cell of the domain, and the percentage error is defined as $100[(\Phi^{\text{harmonic}} - \Phi^{\text{ext}})/\Phi^{\text{ext}}]$, where $\Phi = \eta$ or $\bar{u}$. For each of the panels, the y-axis corresponds to the title. (a) Mean value of elevation [m]; (b) mean value of along-channel velocity [m s^{-1}], and (c) percentage error in the harmonic amplitude of elevation and along-channel velocity.

the theoretical value (Figs. 2c and 3), although, the simulation is stable with no sign of energy growth (Fig. 3). Also, as the phase error increases, an error in the magnitude of the clamped variable develops, up to 40% at 90° (Fig. 2c). The timeseries from the two clamped boundary conditions slightly lag the Flather timeseries (Fig. 3), and comparison with the theoretical solution finds that the Flather condition is the most accurate. Finally, the slight difference in magnitude of every second energy peak for the two clamped boundary conditions is due to the mean offset (Fig. 2a and b).

To address the sensitivity of the three OBCs to errors in amplitude, we conduct a series of simulations where a multiplying factor is applied to either η^{ext} or $\bar{u}^{\text{ext}}$. These simulations apply the same multiplier to both the west and east boundaries, which is similar to assuming that both boundaries were derived from measurements with the same characteristics. Fig. 4 plots the percentage amplitude errors. The two clamped boundary conditions behave as expected. When the multiplier is applied to the variable that is not clamped in one of the clamped OBC (i.e., elevation for the clamped normal velocity OBC or velocity for the clamped elevation OBC), the results are the same as Table 1. Likewise, when the multiplier is applied to the clamped variable the response, in both amplitude and mean offset, is proportional to the change in forcing. Because the Flather condition uses both η^{ext} and $\bar{u}^{\text{ext}}$, it is a little more complicated. The response of the variable which has had the

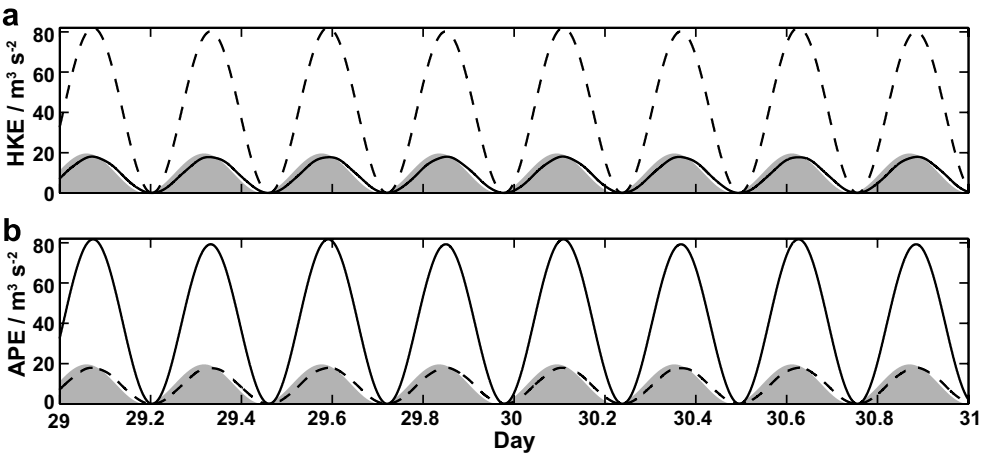

Fig. 3. Time series of (a) horizontal kinetic energy ($\frac{1}{2}H\bar{u}^2$) and (b) available potential energy ($\frac{1}{2}g\eta^2$) at the center grid cell for the last two days of the simulation. This simulation had a +20° phase error. The gray shading gives the results from using the Flather OBC; solid line is the clamped normal velocity OBC; and the dashed line is the clamped elevation OBC.

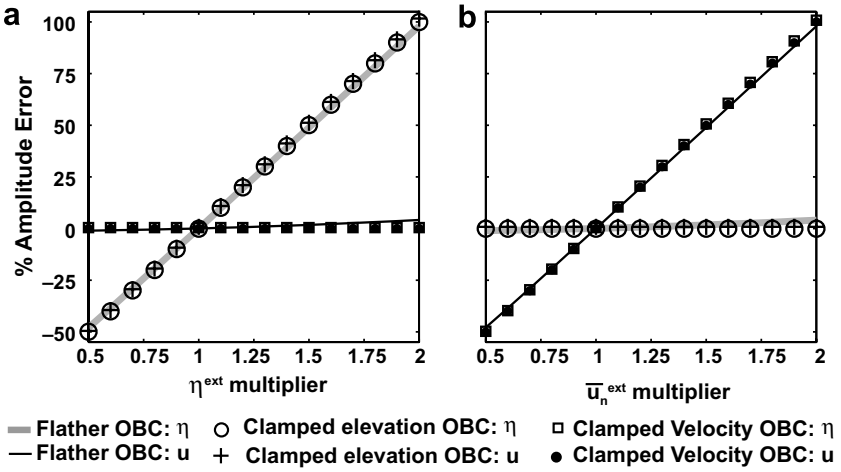

Fig. 4. Sensitivity of tidal simulations to errors in η^{ext} and $\bar{u}^{\text{ext}}$ amplitude. The same multiplier is applied to both the west and east boundary. (a) η^{ext} amplitude varied; and (b) $\bar{u}^{\text{ext}}$ amplitude varied. The symbols are the same as Fig. 2.

multiplier applied is nearly proportional to the multiplier, whereas the other variable only shows a small percentage error. In these tests the Flather simulations show along-channel variability, but the dynamic mismatch between η^{ext} and $\bar{u}^{\text{ext}}$ does not result in any growth or decay with time.

To get an indication of the response to an amplitude error at only one boundary, we conduct simulations where a multiplier of 1.3 is applied to either η^{ext} or $\bar{u}^{\text{ext}}$ at the west boundary while a multiplier of 1.0 is applied to the east boundary. For the clamped elevation condition, the amplitude of the surface elevation oscillations decreases linearly from $1.3\eta^{\text{ext}}$ at the western boundary to $1.0\eta^{\text{ext}}$ at the eastern boundary, while the along-channel velocity amplitude increases nearly linearly from $1.34\bar{u}^{\text{ext}}$ to $1.57\bar{u}^{\text{ext}}$. Over the last 10 tidal cycles the mean value around which the elevation oscillations are centered is slightly negative in the middle of the domain and zero at the end, whereas for the along-channel velocity the mean is -0.005 m s^{-1} over the domain. The results for the clamped velocity simulation are essentially the inverse. The along-channel velocity amplitude decreases from $1.3\bar{u}^{\text{ext}}$ to $1.0\bar{u}^{\text{ext}}$ while the elevation amplitude increases from $1.34\eta^{\text{ext}}$ to $1.57\eta^{\text{ext}}$. The mean elevation value during the last 10 tidal cycles is $+0.025$ m. Neither of the clamped boundary conditions conserves mass with an amplitude error occurring only at one boundary. With the Flather condition the results of applying the multiplier to η^{ext} are identical to applying it to $\bar{u}^{\text{ext}}$. In both cases the elevation and velocity amplitudes are $1.15\eta^{\text{ext}}$ and $1.15\bar{u}^{\text{ext}}$ respectively, and there is no drift in the mean values. If the multiplier is applied to both η^{ext} and $\bar{u}^{\text{ext}}$ then the elevation and velocity amplitudes throughout the domain are consistent with the increased forcing at the western boundary, i.e., $1.3\eta^{\text{ext}}$ and $1.3\bar{u}^{\text{ext}}$.

2.4. Tidal flow at an angle to the domain

In realistic tidal simulations the wave propagation direction will often intersect the boundary at an angle relative to the model grid. Comparison of the three OBCs are performed using a M_2 frequency wave propagating at an angle $\theta = +20°$ to the x-axis. The theoretical solutions in this case are given by (9) and

$$\bar{u} = \eta_0 \sqrt{\frac{g}{H}} \cos(\omega t + \phi) \cos(\theta), \tag{13}$$

$$\bar{v} = \eta_0 \sqrt{\frac{g}{H}} \cos(\omega t + \phi) \sin(\theta). \tag{14}$$

A 170×170 cell domain is used for these simulations, with grid spacing, horizontal viscosity, H, η^{ext} the same as the channel simulations, and (13) and (14) giving $\bar{u}^{\text{ext}}$ and $\bar{v}^{\text{ext}}$ respectively at all open boundaries. The conclusions are similar to the channel case; the Flather OBC is the most accurate and gives very good agreement

Table 2
Comparison of the clamped elevation, clamped normal velocity, and Flather boundary conditions for a constant depth domain where the tide is propagating at an angle to the grid

OBC	η / m		$\bar{u}$ / m s^{-1}		$\bar{v}$ / m s^{-1}	
	Mean	%Error	Mean	%Error	Mean	%Error
Clamped η	Unstable		Unstable		Unstable	
Clamped $\bar{u}_n$	−0.029	0.6	0.000	0.0	0.000	0.0
Flather	0.000	0.0	0.000	0.0	0.000	0.0

Values are from the harmonic analysis on the center cell of the domain. Percentage errors are relative to (9), (13), and (14).

Table 3
Comparison of the clamped elevation, clamped normal velocity, and Flather boundary conditions for a partially standing tide in a constant depth channel (the imposed boundary values are exact)

OBC	η / m			$\bar{u}$ / m s^{-1}		
	Mean	Amp		Mean	Amp	
		Value	%Error		Value	%Error
Clamped η	0.000	2.963	0.0	−0.002	0.052	0.7
Clamped $\bar{u}$	−0.051	2.976	0.4	0.000	0.051	−0.1
Flather	0.000	2.963	0.0	0.000	0.051	0.0

Values are from the harmonic analysis on the center cell of the domain.

with theory (Table 2). However, with zero horizontal viscosity the clamped elevation run becomes unstable. In these tests, like the channel tests, the tangential velocity component is set to zero gradient. Although in this idealized case the tangential velocity is also known exactly, we find setting the tangential velocity directly results in a worse agreement.

Finally, it should be noted that although (13) and (14) collapse to (10) as $\theta \to 0$, only the clamped normal velocity OBC will simulate a channel flow when $\theta = 0$. The reason is that without the normal velocity through the north and south boundaries set to zero, the clamped elevation or Flather OBCs will respond to a change in volume by allowing flow through all four boundaries and hence a non-zero across-channel flow.

2.5. A partially standing tide

Until now we have considered a freely propagating tide, however, in many situations, particularly coastal environments, the surface displacement and velocity are not in phase, i.e., the tide is a partially standing wave. Here we compare the performance of the three OBCs in a channel with a partially standing tide, created as the superposition of an eastward propagating wave ($\eta_1 = a\cos(kx - \omega_{M_2}t),\ a = 2$ m) and a westward propagating wave ($\eta_2 = b\cos(kx + \omega_{M_2}t),\ b = 1$ m). The theoretical solution in this case is

$$\eta = (a+b)\cos(kx)\cos(\omega_{M_2}t) + (a-b)\sin(kx)\sin(\omega_{M_2}t), \tag{15}$$

$$\bar{u} = (a-b)\sqrt{\frac{g}{H}}\cos(kx)\cos(\omega_{M_2}t) + (a+b)\sqrt{\frac{g}{H}}\sin(kx)\sin(\omega_{M_2}t). \tag{16}$$

The results are consistent with the cases considered above. Once again, the Flather condition is the most accurate, while the two clamped conditions give small errors in the unclamped variable (Table 3). With the partially standing wave, there is a −0.1% velocity error with the clamped normal velocity condition, whereas there is no such error with the freely propagating tide (Table 1).

3. Internal mode

The prognostic depth-varying variables within POM are the three velocity components, potential temperature, salinity, turbulent kinetic energy, and a turbulent length scale. In this current investigation the bound-

ary conditions involving these variables need only be passive, i.e., no external information will be transmitted into the domain via them.

For simulations using realistic topography and where internal tide dynamics are important, the internal mode boundary conditions should fulfill the following criteria (with the first two being most important):

(1) The boundary condition does not reflect energy back into the interior domain (i.e., fully transmits or absorbs energy) when a range of vertical modes are present. As noted in Section 1, a significant fraction of the energy can be in mode-2 and higher. This criterion effectively precludes the use of radiation boundary conditions (3), as they assume a single dominant wavespeed. Jensen (1998) suggests decomposing the flow into vertical modes and then applying a radiation condition to each mode separately, but this is very computational expensive.
(2) Realistic topography is included in the boundary region. It is common for baroclinic boundary conditions to be applied over a band of cells, where often the topography is held constant. This can be easily incorporated into idealized test cases used in comparison studies (e.g., Palma and Matano, 2000), but complicates the setting of η^{ext} and $\bar{v}_n^{\text{ext}}$ in simulations with realistic topography.
(3) Kinetic and potential energies are treated similarly. Because the temperature and salinity are dynamically linked to the velocity, dealing with them in a consistent manner in the boundary region may reduce unrealistic secondary flows.
(4) No additional horizontal viscosity is added in the boundary region. Another common approach for increasing stability of the simulation is to add an arbitrarily high viscosity near the boundary, often referred to as a sponge layer.

A modified flow relaxation scheme, presented below, appears to meet all these criteria. Martinsen and Engedahl (1987) originally proposed flow relaxation for barotropic OBCs, with the prognostic variable Φ, near the boundary, being given as

$$\Phi = \alpha\Phi^{\text{ext}} + (1-\alpha)\Phi^{*}, \tag{17}$$

where Φ^{*} denotes a time-integrated value calculated by the model, and α is a relaxation parameter that varies from 0 to 1. This scheme is designed to absorb the outgoing energy, in contrast to the Flather barotropic condition which transmits the energy. Following Martinsen and Engedahl (1987) we define α as $\alpha(i) = 1 - \tanh[\frac{1}{2}(i-1)]$ where i is an index over the width of the relaxation layer.

Flow relaxation schemes have often been used in conjunction with other temperature and salinity boundary conditions, such as radiation (Blumberg and Kantha, 1985; Cummins et al., 2001) or advection (Holloway and Merrifield, 2003), to damp out energy not accounted for by the primary boundary condition. Marchesiello et al. (2001) applied flow relaxation (nudging) to all variables except elevation. When the boundary was passive they combined weak relaxation with oblique radiation, and when the boundary was active they used strong relaxation. In one of their tests, Palma and Matano (2000) used a pure flow relaxation scheme for temperature and salinity when the flow was into the domain. Jensen (1998) reports excellent results using a flow relaxation scheme to radiate one-dimensional internal waves out of a three-layer z-coordinate model. However, he cautioned that the solution being relaxed towards must be chosen carefully to obtain good results.

3.1. Implementation of internal mode boundary condition

Although, we use a flow relaxation scheme for all the internal mode variables there are important differences in their implementation. Accordingly, we discuss them separately.

3.1.1. Horizontal velocity

The two horizontal velocity components are relaxed to the corresponding depth-averaged values. This is equivalent to relaxing the baroclinic fluctuation to zero. Although POM utilizes mode splitting the internal mode velocities include the depth-averaged component.

Because the topography is allowed to vary in the relaxation region, there is no reason to presume that depth-averaged velocity at the boundary is relevant to a cell within the relaxation region. For instance, in

the extreme consider a island cutting through the relaxation region at an angle. Consequently, we relax to the depth-averaged velocity calculated in that cell, i.e.,

$$u(i,j,k) = \alpha\bar{u}(i,j) + (1-\alpha)u^*(i,j,k) \quad \text{and} \quad v(i,j,k) = \alpha\bar{v}(i,j) + (1-\alpha)v^*(i,j,k), \tag{18}$$

where i, j, k are indexes in the x, y, z directions respectively.

3.1.2. Isopycnal displacement (potential temperature and salinity)

The isopycnal displacement is relaxed to zero. By reducing the displacement at the same rate (α) as the baroclinic velocities, the density field does not become decoupled from the velocity field. Because the model variables are potential temperature and salinity, the reduced isopycnal displacement is mapped back into these variables. If the temperature and salinity are relaxed individually, instabilities can arise, particularly over variable topography, because density is the dynamically relevant variable, and the equation of state linking temperature and salinity to density is non-linear.

We find the best approach is to relax the displacement along the original smooth high-resolution temperature and salinity profiles. Because the salinity profile can be multi-valued, and the thermocline and halocline displacements should be the same (driven by the same vertical velocities), the displacement is defined using temperature. The displacement is then simply the difference between the depth of a given cell and the depth of the corresponding temperature in the high-resolution profile. The displacement is then relaxed using (17) with $\Phi^{\text{ext}} = 0$. The new temperature and salinity values are then obtained for this relaxed depth from the high-resolution profiles.

Although the potential temperature and salinity are relaxed using the high-resolution profiles, simulations with strong thermoclines (like that shown in Fig. 5b) still require a reasonably large number of sigma levels. This is because the advection calculation works best when the difference between levels is not extreme. For example, if only 11 sigma levels were used with this temperature profile, there would be over 10 °C difference between levels 1 and 2.

3.1.3. Vertical velocity, and turbulence quantities

The vertical velocity and turbulent kinetic energy are relaxed to zero. Because of the way the turbulent length scale is implemented in POM, it appears in a denominator, it is relaxed to a small, but non-zero, value.

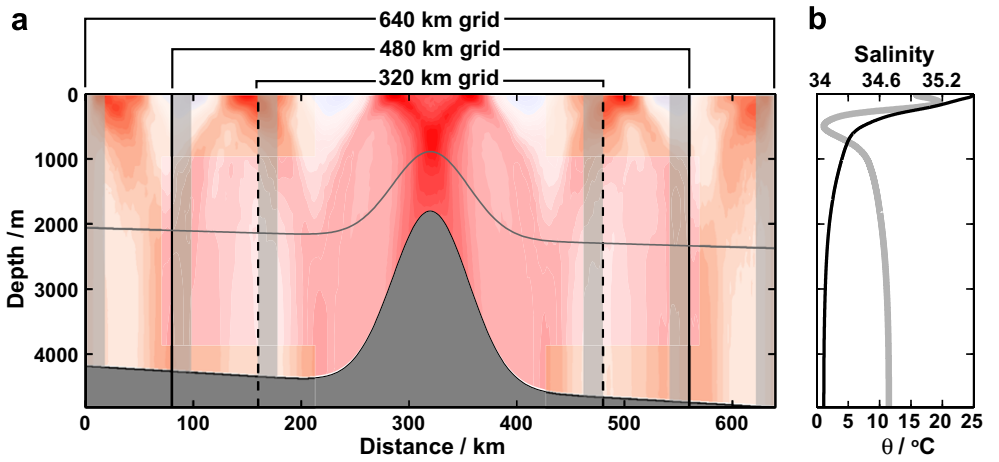

Fig. 5. (a) Along-channel topography for the three domains used to illustrate the performance of the modified flow relaxation scheme. The vertical solid and dashed lines show the boundaries of the three domains, and the light gray patches give the location of the relaxation regions. The u velocity (M_2-only forcing) after 356.5 h of integration is plotted in the background, and clearly shows internal tide beams throughout the domain. The gray line gives the location of the sigma level used in Fig. 6. (b) Ten year average of potential temperature and salinity from Station Aloha.

3.2. Performance of the modified flow relaxation scheme

3.2.1. Comparison between domains of different lengths

To illustrate the performance of the modified flow relaxation scheme presented above, simulations with different domain lengths are compared for a channel with a central ridge and sloping bottom (Fig. 5a). A 2700 m high Gaussian ridge is superimposed on a domain with 4500 m mean depth and a −1:1000 slope. The linear sloping bottom is used to give topographic variation within the relaxation regions (criteria 2), while minimizing additional internal tide generation in the larger domains. For the same reason, the smallest domain encompasses the entire ridge. The temperature and salinity profiles (Fig. 5b), an average of 10 years of data from the Hawaii Ocean Time Series experiment at Station Aloha, include a sharp thermocline and salinity inversions.

Two sets of simulations are presented. The first is forced with a $\eta^{\text{ext}} = 1$ m amplitude M_2 frequency wave. The second is forced with the six main tidal constituents, and the amplitudes are consistent with their global amplitudes relative to a M_2 elevation of 1 m ($M_2 = 1$ m; $S_2 = 0.47$ m; $N_2 = 0.19$ m; $K_1 = 0.58$ m; $O_1 = 0.42$ m; and $P_1 = 0.19$ m; Pugh, 1987). All simulations have a 2 km horizontal resolution, 71 sigma levels in the vertical, and were forced using the Flather OBC. To minimize the differences in forcing, the phase at the western boundary is calculated by (11) relative to the 480 km domain. Each simulation is spun up from a quiescent state over one day. The horizontal viscosity term is set to zero, and the relaxation regions are 10 cells wide. A time slice of along-channel velocity (after 356.5 h, M_2-only forcing) clearly shows that internal tidal beams are formed and are coherent through the domain (Fig. 5a). As mentioned above the presence of tidal beams requires a range of vertical modes.

Comparisons of the baroclinic component of the along-channel velocity $(u - \bar{u})$ for sigma level 35 (location of which is shown in Fig. 5a) are shown for the M_2-only case (Fig. 6) and the six constituent forcing case (Fig. 7). During the spin up period, and as the gravest mode reaches the boundary of the smallest domain the agreement is extremely good (Fig. 6a). After the initial spin up, the agreement degrades slightly but remains very good. Figs. 6b and c, and 7a illustrate a reoccurring theme, that the largest differences between the domains are over the ridge crest. This suggests that small differences in forcing account for a substantial fraction of the variation between the simulations. At certain phases of the tide, the overall agreement is worse (e.g., Figs. 6c and 7a) than at others (e.g., Figs. 6d and 7b). A potential explanation for this may be the problem of specifying a depth-averaged flow over sloping topography as the "barotropic" component. The increase in high frequency variation in Fig. 6c and d compared to Fig. 6a and b is due to the higher modes taking longer to propagate through the domain. From flat-bottom baroclinic modes calculated using the stratification in Fig. 5b, the mode-10 propagation speed is $0.35\ \text{m s}^{-1}$ compared to $3.24\ \text{m s}^{-1}$ for mode-1 and $1.72\ \text{m s}^{-1}$ for mode-2. As the baroclinic velocities from the shorter domains follow those from the longest domain even when high modes and multiple constituents are present, we conclude that no significant amount of energy has been reflected and, therefore, criteria 1 has been meet.

In free surface models the application of boundary conditions can lead to mass not being conserved, unless an artificial volume constraint is included (e.g., Palma and Matano, 1998; Marchesiello et al., 2001). To assess the modified flow relaxation scheme in terms of mass conservation, we compare mean sealevel for the M_2 forced 640 km domain between a 30 tidal cycle simulation and a 130 tidal cycle simulation. Mean sealevel is calculated over the last 10 tidal cycles of each simulation. In both cases the mean sealevel is less than a millimeter different from the initial, zero, value. Consequently, no volume constraint is required.

3.2.2. Comparison to the Pétrélis et al. (2006) analytical solution

Pétrélis et al. (2006) present an analytical expression for tidal conversion in a uniformly stratified fluid over a two-dimensional submarine ridge. This solution collapses to the knife-edge solution (Llewellyn-Smith and Young, 2002; St Laurent and Garrett, 2002) at the supercritical limit and to the Bell (1975a,b) solution for weak topography. The conversion in W m^{-1} (of along-ridge extent) is

$$C = \frac{1}{4}\pi\rho_0 U_0^2 N b^2 \sqrt{1 - \left(\frac{f}{\omega}\right)^2} \times M\left(\frac{\mu a}{H}, \frac{b}{H}\right), \tag{19}$$

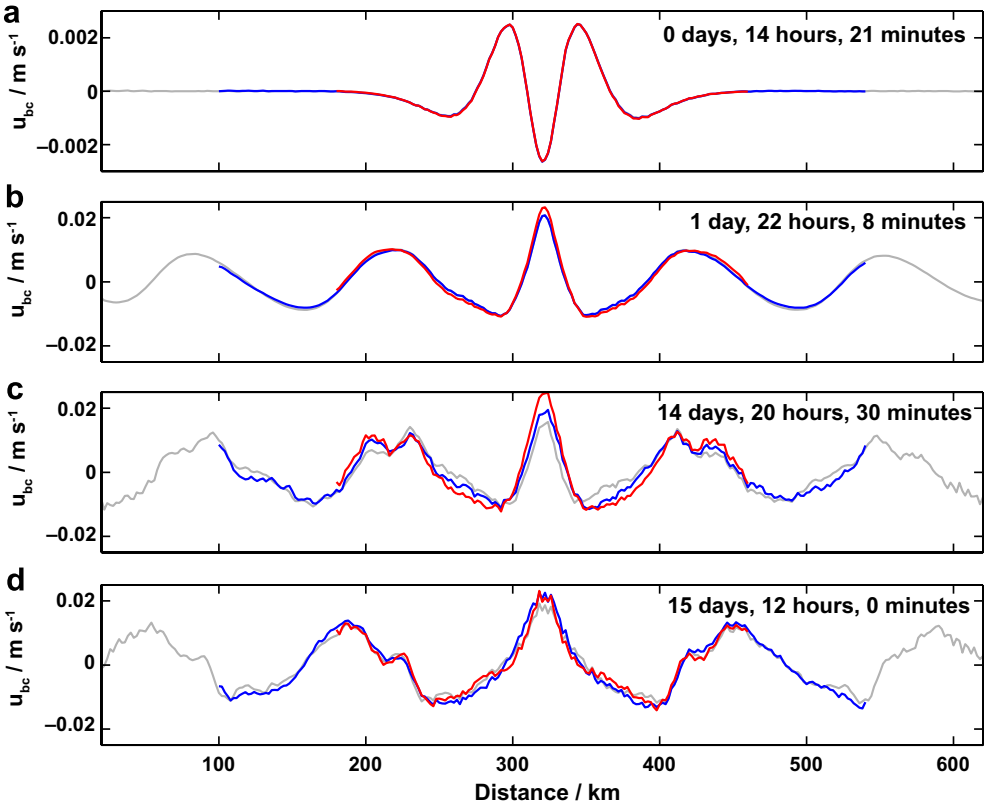

Fig. 6. Comparison of the baroclinic component of along-channel velocity $(u - \bar{u})$ for the M_2-only forcing case. The velocities are from sigma level 35, marked in Fig. 5a. The gray line is the 640 km long domain, the blue line is the 480 km long domain, and the red line is the 320 km long domain. Velocities within the relaxation layers have not been plotted. The integration time of the comparison is given in each panel. Note the different scale on panel (a).

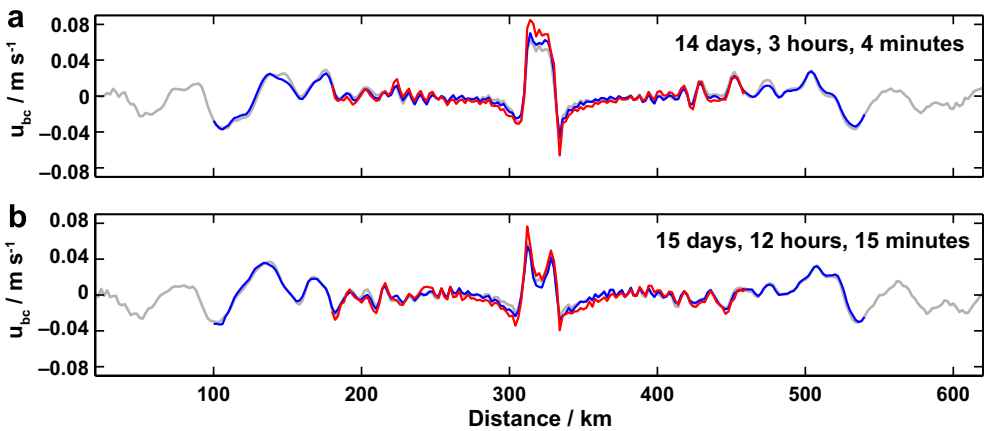

Fig. 7. Comparison of the baroclinic component of along-channel velocity $(u - \bar{u})$ for the six constituent forcing case. The velocities are from sigma level 35, marked in Fig. 5a. The gray line is the 640 km long domain, the blue line is the 480 km long domain, and the red line is the 320 km long domain. Velocities within the relaxation layers have not been plotted. The integration time of the comparison is given in each panel.

where U_0^2 is the velocity amplitude away from the ridge, N is the buoyancy frequency, b is the ridge height, a is the half-width of the ridge, and $\mu = N/\sqrt{\omega^2 - f^2}$ is the inverse characteristic slope. $M\left(\frac{\mu a}{H}, \frac{b}{H}\right)$ is a dimensionless parameter, which we evaluate following Pétrélis et al. (2006) for a polynomial ridge defined by

$$z = -H + b\begin{cases} \left(1 - \frac{x^2}{a^2}\right)^2 & \text{if } |x| < a, \\ 0 & \text{if } |x| > a. \end{cases} \tag{20}$$

As a check on the performance of the modified relaxation scheme, we compare the modeled barotropic-to-baroclinic conversion to the Pétrélis solution. Di Lorenzo et al. (2006) found what they describe as satisfactory agreement between the analytical solution and conversion estimates from the Regional Ocean Modeling System (ROMS). In those simulations Di Lorenzo et al. (2006) used periodic boundary conditions on a 1200 km long domain, but limited the integration time to 12 tidal cycles, less than the travel time for the mode 1 internal tide to the boundary (i.e., no baroclinic energy reaches the boundaries, so the nature of the boundary conditions is irrelevant). When they simulated a shorter domain, the baroclinic energy propagated back into the domain leading to zero energy flux.

We consider a series of simulations of a polynomial ridge of half-width 10 km with the fractional height of the ridge (b/H) ranging from 0.1 to 0.8. All simulations are on a 1200 km long domain, and have a M_2 tidal frequency, $U_0 = 2$ cm s^{-1}, $H = 2000$ m, $f = 0$, $N = 1.7 \times 10^{-3}$ s^{-1}. To isolate the role of the boundary conditions we compare results from runs with a 12 tidal cycle integration time (no baroclinic energy reaches the boundary) to runs with a 100 tidal cycle integration time. The energy flux is an average over the last four tidal cycles. The agreement between the 12 tidal cycle runs and analytical conversion is consistent with Di Lorenzo et al. (2006) (Fig. 8a and b), with mean difference being −3.5% and standard deviation of 2.9%. The difference in conversion between the 12 and 100 tidal cycle runs is small (mean = 0.1%, standard deviation = 4.6%), and has no relation to b/H (gray bars in Fig. 8b).

A further verification of the modified relaxation scheme for internal tide studies is obtained by considering along-channel sections of baroclinic energy flux as a function of integration time (Fig. 8c). As expected after 12 tidal cycles no baroclinic energy has reached the boundary, by 24 tidal cycles some higher mode energy still has not reach the boundary. The 50, 100, and 200 tidal cycle lines all lie almost on top of each other (percentage error $\lesssim$0.1%), clearly indicating no energy build up within the domain. Between the 24 and 50 tidal cycle runs, there is a slight decrease in the peak energy fluxes resulting in the −8.2% difference seen in Fig. 8b for the

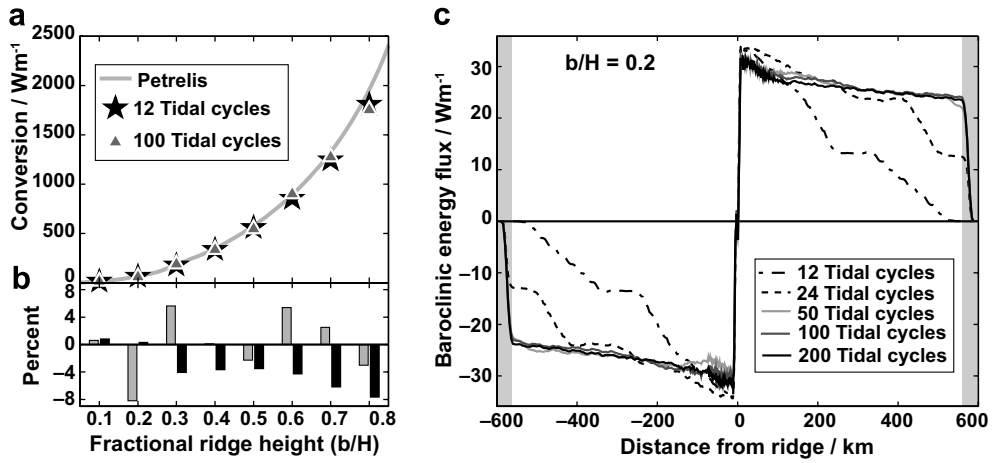

Fig. 8. (a) Model estimates of conversion after 12 tidal cycles of integration (stars), and after 100 tidal cycles of integration (triangles) compared to the Pétrélis et al. (2006) analytical solution. (b) The gray bars show the percentage difference between conversion calculated from the 12 and 100 tidal cycle simulations. The black bars are the percentage differences between the 12 tidal cycle model conversions and the analytical solution. (c) Along-channel baroclinic energy flux for the case when $b/H = 0.2$, where there was the worst agreement between the 12 and 100 tidal cycle simulations. Integration times of 12, 24, 50, 100, and 200 tidal cycles are compared. The gray shading shows the extent of the relaxation regions.

$b/H = 0.2$ case. The longer integration runs show some noise close to the ridge, but the magnitude and horizontal extent of this noise does not appear to increase with integration time. A possible cause of this noise maybe the pressure gradient error associated with sigma coordinate models, Di Lorenzo et al. (2006) discuss other possible errors in the comparison.

4. Discussion and conclusions

Three external mode (depth-averaged) open boundary conditions commonly used in regional tidal simulations are compared using a simple flat-bottom channel. All three (clamped elevation, clamped normal velocity, and Flather) gave good agreement to theory when the boundary conditions are exact; however, the Flather condition is the least sensitive to errors in the prescribed boundary values. Of particular concern, we found that with a phase error between the two boundaries, both the clamped conditions result in magnitude errors in the unclamped variable (although the simulation remained stable). With a 1° phase error the modeled amplitude is out by ~5%, and by a 20° phase error the amplitude is twice the theoretical value.

Consequently, we recommend using Flather for the external mode boundary condition, which requires both η^{ext} and $\bar{v}_n^{\text{ext}}$. Satellite constrained global inverse models (e.g., Egbert and Erofeeva, 2002) can provide both these components, however, there are two common sources of inaccuracies to be aware of. First, when using a basin scale model to force a smaller scale regional model, the domains often incorporate different resolution topography which can lead to mismatches in the tidal variables at the common boundaries. Selection of the boundary location to be over slowly varying topography can minimize this error. Second, the velocity tends to become noisy in shallow water. Flather (1987) used a two-step process involving only elevation data. A short simulation was performed using clamped elevation boundary conditions, and amplitude and phase were then calculated for the modeled velocity at the open boundary. The final simulation was driven by the Flather condition using satellite elevations and modeled velocities. We did not evaluate this two-step process but the potential errors can be estimated from the sensitivity analysis presented in Figs. 2 and 4.

At least in tidal process studies, a modified flow relaxation scheme is found to be an excellent boundary condition for the internal (depth-varying) mode prognostic variables. This implementation allows the transmission of a range of vertical modes while retaining realistic topography at the boundary. The performance was tested by comparing simulations of different domain length encompassing a ridge and sloping bottom, and by comparison to the analytical solution of Pétrélis et al. (2006). Both tests demonstrated that this boundary condition handled well formed tidal beams without reflection or energy build up. Comparison of simulations over 30 and 130 tidal cycles show that mass is conserved without any artificial volume constraint.

The applicability of a set of boundary conditions can be dependent on the model/problem configuration. Therefore, we have limited this investigation to the area that initially motivated it, the dynamics of internal tides. Although it is beyond the scope of this current study to test these boundary conditions using different problem configurations, we will close with a few comments about their extension. The most likely extension would be to simulate a combination of tidal and subtidal processes. The obvious difficulty in extending the boundary condition presented here is to know what to relax towards. As far as internal tides are concerned the important factor is to relax to zero the baroclinic fluctuations in velocity and isopycnal displacement. In the current case this is achieved by relaxing the depth-varying velocity to the depth-averaged velocity. However, for example, in a case where there is a time-invariant surface jet as well as tidal processes, then it seems that relaxing to a superposition of the jet structure and the barotropic tide will fulfill the requirement of no reflection of internal tide energy at the boundary.

Acknowledgements

The authors wish to thank the two anonymous reviewers. The work was funded by the National Science Foundation (NSF) under contract OCE0425347. The temperature and salinity data from Station ALOHA is supplied by the Hawaii Ocean Timeseries program (NSF grants OCE9303094, 9811921, 0117919, and 0327513).

References

Banas, N.S., Hickey, B.M., 2005. Mapping exchange and residence time in a model of Willipa Bay, Washington, a branching, macrotidal estuary. Journal of Geophysical Research 110, C11011. doi:10.1029/2005JC002950.

Bell, T.H., 1975a. Lee waves in stratified fluid with simple harmonic time dependence. Journal of Fluid Mechanics 67, 705–722.

Bell, T.H., 1975b. Topographically generated internal waves in the open ocean. Journal of Geophysical Research 80, 320–327.

Black, K.P., Bell, R.G., Oldman, J.W., Carter, G.S., Hume, T.M., 2000. Features of 3-dimensional barotropic and baroclinic circulation in the Hauraki Gulf, New Zealand. New Zealand Journal of Marine and Freshwater Research 34, 1–28.

Blayo, E., Debreu, L., 2005. Revisiting open boundary conditions from the point of view of characteristic variables. Ocean Modelling 9, 231–252.

Blumberg, A.F., Kantha, L.H., 1985. Open boundary condition for circulation models. Journal of Hydraulic Engineering 111 (2), 237–255.

Blumberg, A.F., Mellor, G.L., 1987. A description of a three-dimensional coastal ocean circulation model. In: Heaps, N.S. (Ed.), Three-Dimensional Coastal Ocean Models, . In: Coastal and Estuarine Sciences, vol. 4. American Geophysical Union, Washington, DC, pp. 1–16.

Carter, G.S., Gregg, M.C., Merrifield, M.A., 2006. Flow and mixing around a small seamount on Kaena Ridge, Hawaii. Journal of Physical Oceanography 36 (6), 1036–1052.

Chapman, D.C., 1985. Numerical treatment of cross-shelf open boundaries in a barotropic coastal ocean model. Journal of Physical Oceanography 15 (8), 1060–1075.

Cheng, R.T., Casulli, V., Gartner, J.W., 1993. Tidal, residual, intertidal mudflat (TRIM) model and its applications to San Francisco Bay, California. Estuarine, Coastal and Shelf Science 36, 235–280.

Cummins, P.F., Cherniawsky, J.Y., Foreman, M.G.G., 2001. North Pacific internal tides from the Aleutian Ridge: Altimeter observations and modeling. Journal of Marine Research 59, 167–191.

Di Lorenzo, E., Young, W.R., Llewellyn Smith, S., 2006. Numerical and analytical estimates of m_2 tidal conversion at steep oceanic ridges. Journal of Physical Oceanography 36 (6), 1072–1084.

Dushaw, B.D., Cornuelle, B.D., Worcester, P.F., Howe, B.M., Luther, D.S., 1995. Barotropic and baroclinic tides in the Central North Pacific Ocean determined from long-range reciprocal acoustic transmissions. Journal of Physical Oceanography 25 (4), 631–647.

Egbert, G.D., Erofeeva, S.Y., 2002. Efficient inverse modeling of barotropic ocean tides. Journal of Atmospheric and Oceanic Technology 19 (2), 183–204.

Egbert, G.D., Ray, R.D., 2000. Significant dissipation of tidal energy in the deep ocean inferred from satellite altimeter data. Nature 405, 775–778.

Egbert, G.D., Ray, R.D., 2001. Estimates of M_2 tidal energy dissipation from TOPEX/Poseidon altmeter data. Journal of Geophysical Research 106 (C10), 22,475–22,502.

Flather, R.A., 1976. A tidal model of the north-west European continental shelf. Memoires de la Societe Royale des Sciences de Liege 6 (10), 141–164.

Flather, R.A., 1987. A tidal model of the Northeast Pacific. Atmosphere-Ocean 25 (1), 22–45.

Garrett, C., Kunze, E., 2007. Internal tide generation in the deep ocean. Annual Review of Fluid Mechanics 39, 57–87.

Holloway, P.E., 1996. A numerical model of internal tides with application to the Australian North West Shelf. Journal of Physical Oceanography 26 (1), 21–37.

Holloway, P.E., Merrifield, M.A., 1999. Internal tide generation by seamounts, ridges, and islands. Journal of Geophysical Research 104 (C11), 25,937–25,951.

Holloway, P.E., Merrifield, M.A., 2003. On the spring-neap variability and age of the internal tide at the Hawaiian Ridge. Journal of Geophysical Research 108 (C4), 3126. doi:10.1029/2002JC001486.

Jensen, T.G., 1998. Open boundary conditions in stratified ocean models. Journal of Marine Systems 16, 297–322.

Johnston, T.M.S., Merrifield, M.A., 2003. Internal tide scattering at seamounts, ridges, and islands. Journal of Geophysical Research 108 (C6), 3180. doi:10.1029/2002JC001528.

Johnston, T.M.S., Merrifield, M.A., Holloway, P.E., 2003. Internal tide scattering at the Line Islands. Journal of Geophysical Research 108 (C11), 3365. doi:10.1029/2003JC001844.

Katsumata, K., 2005. Two- and three-dimensional numerical models of internal tide generation at a continental slope. Ocean Modelling 12 (1–2), 32–45.

Klymak, J.M., Moum, J.N., Nash, J.D., Kunze, E., Girton, J.B., Carter, G.S., Lee, C., Sanford, T.B., Gregg, M.C., 2006. An estimate of energy lost to turbulence at the Hawaiian Ridge. Journal of Physical Oceanography 36 (6), 1148–1164.

Lee, C.M., Kunze, E., Sanford, T.B., Nash, J.D., Merrifield, M.A., Holloway, P.E., 2006. Internal tides and turbulence along the 3000-m isobath of the Hawaiian Ridge with model comparison. Journal of Physical Oceanography 26 (6), 1165–1183.

Llewellyn-Smith, S.G., Young, W.R., 2002. Conversion of the barotropic tide. Journal of Physical Oceanography 32, 1554–1566.

Marchesiello, P., McWilliams, J.C., Shchepetken, A., 2001. Open boundary conditions for long-term integration of regional oceanic models. Ocean Modelling 3, 1–20.

Martinsen, E.A., Engedahl, H., 1987. Implementation and testing of a lateral boundary scheme as an open boundary condition in a barotropic ocean model. Coastal Engineering 11, 603–627.

Mellor, G.L., 2004. User's guide for a three-dimensional, primitive equation, numerical ocean model. Program in Atmospheric and Oceanic Sciences, Princeton University, Princeton, NJ 08544-0710.

Merrifield, M.A., Holloway, P.E., 2002. Model estimates of M_2 internal tide energetics at the Hawaiian Ridge. Journal of Geophysical Research 107 (C8). doi:10.1029/2001JC000996.

Merrifield, M.A., Holloway, P.E., Johnston, T.M.S., 2001. The generation of internal tides at the Hawaiian Ridge. Geophysical Research Letters 28 (4), 559–562.

Niwa, Y., Hibiya, T., 2001. Numerical study of the spatial distribution of the M_2 internal tide in the Pacific Ocean. Journal of Geophysical Research 106 (C10), 22,441–22,449.

Oliger, J., Sundström, A., 1978. Theoretical and practical aspects of some initial boundary value problems in fluid dynamics. SIAM Journal on Applied Mathematics 35 (3), 419–446.

Palma, E.D., Matano, R.P., 1998. On the implementation of passive open boundary conditions for a general circulation model: the barotropic mode. Journal of Geophysical Research 103 (C1), 1319–1341.

Palma, E.D., Matano, R.P., 2000. On the implementation of open boundary conditions for a general circulation model: the three-dimensional case. Journal of Geophysical Research 105 (C4), 8605–8627.

Pétrélis, F., Llewellyn Smith, S., Young, W.R., 2006. Tidal conversion at a submarine ridge. Journal of Physical Oceanography 36 (6), 1053–1071.

Pinkel, R., Munk, W., Worcester, P., Cornuelle, B.D., Rudnick, D., Sherman, J., Filloux, J.H., Dushaw, B.D., Howe, B.M., Sanford, T.B., Lee, C.M., Kunze, E., Gregg, M.C., Miller, J.B., Moum, J.M., Caldwell, D.R., Levine, M.D., Boyd, T., Egbert, G.D., Merrifield, M.A., Luther, D.S., Firing, E., Brainard, R., Flament, P.J., Chave, A.D., 2000. Ocean mixing studied near Hawaiian Ridge. EOS, Transactions, American Geophysical Union 81 (46), 545–553.

Press, W.H., Flannery, B.P., Teukolsky, S.A., Vetterling, W.T., 1989. Numerical Recipes: The Art of Scientific Computing (FORTRAN Version). Cambridge University Press.

Prinsenberg, S.J., Wilmot, W.L., Rattary, M., 1974. Generation and dissipation of coastal internal tides. Deep-Sea Research I 21, 263–281.

Pugh, D.T., 1987. Tides, Surges and Mean Sea-Level. John Wiley & Sons, 472 pp.

Ray, R.D., Mitchum, G.T., 1996. Surface manifestation of internal tides generated near Hawaii. Geophysical Research Letters 23, 2101–2104.

Rudnick, D.L., Boyd, T.J., Brainard, R.E., Carter, G.S., Egbert, G.D., Gregg, M.C., Holloway, P.E., Klymak, J.M., Kunze, E., Lee, C.M., Levine, M.D., Luther, D.S., Martin, J.P., Merrifield, M.A., Moum, J.N., Nash, J.D., Pinkel, R., Rainville, L., Sanford, T.B., 2003. From tides to mixing along the Hawaiian Ridge. Science 301, 355–357.

St Laurent, L.C., Garrett, C.J.R., 2002. The role of internal tides in mixing the deep ocean. Journal of Physical Oceanography 32, 2882–2899.

St Laurent, L.C., Simmons, H.L., Jayne, S.R., 2002. Estimating tidally driven mixing in the deep ocean. Geophysical Research Letters 29 (23), 2106. doi:10.1029/2002GL015633.